

PAPER

Photoacoustic imaging of 3D-printed vascular networks

To cite this article: Chenshuo Ma et al 2022 Biofabrication 14 025001

View the article online for updates and enhancements.

You may also like

- Shifts of pNIPAM Lower Critical Solution Temperature in an Applied Electric Field Jeffrey M Halpern, Emma Roberge, Tianyu Ren et al.
- (Invited) Diamond Electrodes for Sensitive Electrochemical Detection T. Kondo
- <u>Atomic-scale Dopant Integration During</u>
 <u>CMOS Device Fabrication</u>
 Andrew Leenheer, Connor Halsey, Daniel
 Ward et al.



Breath Biopsy® OMNI

The most advanced, complete solution for global breath biomarker analysis





Expert Study Design & Management



Robust Breath Collection



Reliable Sample Processing & Analysis



n-depth Data Analysis



Interpretation

Biofabrication



RECEIVED

19 September 2021

REVISED

23 December 2021

ACCEPTED FOR PUBLICATION
10 January 2022

PUBLISHED
24 January 2022

PAPER

Photoacoustic imaging of 3D-printed vascular networks

Chenshuo Ma^{1,4}, Wanlu Li^{2,4}, Daiwei Li¹, Maomao Chen¹, Mian Wang², Laiming Jiang³, Luis Santiago Mille², Carlos Ezio Garciamendez², Zhibo Zhao², Qifa Zhou³, Yu Shrike Zhang^{2,*} and Junjie Yao^{1,*}

- Department of Biomedical Engineering, Duke University, Durham, NC 27708, United States of America
- ² Division of Engineering in Medicine, Department of Medicine, Brigham and Women's Hospital, Harvard Medical School, Cambridge, MA 02139, United States of America
- Department of Biomedical Engineering and USC Roski Eye Institute, University of Southern California, Los Angeles, CA 90007, United States of America
- ⁴ These authors contributed equally.
- * Authors to whom any correspondence should be addressed.

E-mail: yszhang@research.bwh.harvard.edu and junjie.yao@duke.edu

Keywords: photoacoustic imaging, photoacoustic microscopy, bioprinting, digital light processing, blood oxygenation Supplementary material for this article is available online

Abstract

Thrombosis in the circulation system can lead to major myocardial infarction and cardiovascular deaths. Understanding thrombosis formation is necessary for developing safe and effective treatments. In this work, using digital light processing (DLP)-based 3D printing, we fabricated sophisticated *in vitro* models of blood vessels with internal microchannels that can be used for thrombosis studies. In this regard, photoacoustic microscopy (PAM) offers a unique advantage for label-free visualization of the 3D-printed vessel models, with large penetration depth and functional sensitivity. We compared the imaging performances of two PAM implementations: optical-resolution PAM and acoustic-resolution PAM, and investigated 3D-printed vessel structures with different patterns of microchannels. Our results show that PAM can provide clear microchannel structures at depths up to 3.6 mm. We further quantified the blood oxygenation in the 3D-printed vascular models, showing that thrombi had lower oxygenation than the normal blood. We expect that PAM can find broad applications in 3D printing and bioprinting for *in vitro* studies of various vascular and other diseases.

1. Introduction

Thrombosis is the principal cause of cardiovascularrelated diseases [1, 2], which may also play a role in the development of cancers [3]. For example, ischemic stroke, which affects more than 0.7 million Americans each year [4], occurs when a thrombus shuts off an artery supplying blood to the brain. About 87% of stroke incidences are ischemic stroke in the brain [5], and most heart attacks are caused by acute arterial thrombosis [6]. In order to study thrombosis-induced diseases and develop effective treatment regimes, it is highly important to develop biological models that can be used for precisely monitoring the blood clot formation.

Three-dimensional (3D) printing as an emerging technology for biomedical applications, provides

the possibility of building vascular constructs with complex geometrical, molecular, and cellular features based on digital files [7-11]. 3D-printed microchannels allow the emulation of blood vessels, enabling in vitro thrombosis studies. Digital light processing (DLP)-based 3D printing utilizes patterns projected from the digital micromirror device (DMD) or liquid crystal display (LCD) to photopolymerize the liquid ink into volumetric constructs in a layer-bylayer manner [11-14]. Compared with other nozzlebased printing approaches such as those using the extrusion mechanism, DLP-based 3D printing shows superiority in printing resolution at the micrometer scale [12, 14-19]. Additionally, DLP-based 3D printing enables a higher printing speed when projecting an entire two-dimensional (2D) pattern each time, instead of the point-by-point laser scanning in stereolithography apparatus (SLA)-based printing [20]. Furthermore, using clinical image data as printing files, DLP-based 3D printing can produce patient-specific scaffolds for tissue modeling, tissue regeneration, and medical devices [21–24]. Thus, with high resolution, high speed, and rich design flexibility, DLP-based 3D printing has great potential in the rapid fabrication of sophisticated structures such as vascular and thrombosis models.

On the other hand, it is oftentimes necessary to image the internal structures of 3D-printed samples for accurate analyses of structural and functional information. However, the bulky volumes of most printed constructs and the optical properties of the tissue-mimicking hydrogel materials usually result in strong optical scattering and/or absorption, which makes it challenging to use high-resolution optical microscopy that is plagued by the limited imaging depth [25, 26]. For example, the imaging depth of confocal microscopy is limited to 100–200 μ m [27]. Two-photon microscopy improves the imaging depth by using longer excitation wavelengths, which reduces optical attenuation and broadens optical focusing, but the imaging depth remains at around 1 mm. Different from other optical imaging technologies, photo-acoustic microscopy (PAM), a hybrid imaging modality that acoustically detects optical absorption contrast via the photo-acoustic (PA) effect, achieves relatively deep penetration with scalable spatial resolutions, because biological tissue is orders of magnitude more transparent to sound than to light [28, 29]. PAM has been widely used for imaging single cells [30–32], microvasculature [33, 34], organs [35], brain activities [36, 37], blood flow [38–40], oxygen saturation of hemoglobin (sO_2) [41], molecular labels [42-45], and tumors [46]. There are two major PAM implementations: (1) in optical-resolution PAM (OR-PAM), the excitation is tightly focused, and the penetration depth can reach 1 mm; (2) in acoustic-resolution PAM (AR-PAM), the excitation light is only loosely focused to fulfill the entire acoustic detection volume and the lateral resolution is determined by ultrasonic focusing at depths of a few transports mean free paths [47]. The penetration depth of AR-PAM can reach 5 mm.

In this work, we have demonstrated that both OR-PAM and AR-PAM are capable of imaging various 3D-printed vascular and thrombosis models. Compared with OR-PAM, AR-PAM can achieve deeper penetration and facilitate better visualization of volumetric structures. PAM can differentiate oxyhemoglobin (HbO₂) and deoxy-hemoglobin (HbR), and thus can quantitatively measure the blood oxygenation of the thrombosis [48]. Overall, PAM may become a useful tool for studying the morphologies and functions of 3D-printed/bioprinted constructs for thrombosis studies and beyond.

2. Methods

2.1. Synthesizing gelatin methacryloyl (GelMA) and hyaluronic acid methacrylate (HAMA)

GelMA was synthesized according to previously reported method [24, 48–50]. In brief, gelatin from cold-water fish skin (10 g, Sigma-Aldrich, USA) was dissolved in phosphate-buffered saline (PBS, ThermoFisher, USA; 100 ml) at the concentration of 10 wt.%. Methacrylic anhydride (MA, Sigma-Aldrich; 12 ml) was then added dropwise and was reacted with gelatin solution at 50 °C for 2 h. After diluting the solution at 1:1 with warm PBS (40 °C) to stop the reaction, dialysis was conducted for 7 d against de-ionized (DI) water using dialysis membrane (molecular weight cut off = 12-14 kDa, Spectrum Chemical, USA) at 40 °C to remove low-molecular weight impurities. Subsequently, the solution was lyophilized and stored at -20 °C in dark until use.

The synthesis of HAMA followed the procedure as previously described [50]. Briefly, 4.0 g of hyaluronic acid (molecular weight = 500 kDa) was fully dissolved in 200 ml of DI water at 4 °C. A total of 133.3 ml of dimethylformamide (DMF, Sigma-Aldrich) and 7.88 ml of MA were added into HA solution under vigorous stirring. The pH of the solution was regulated to pH 8-9 with 1 M sodium hydroxide (Sigma-Aldrich) solution. The reaction was kept at 4 °C under continuous stirring for another 18 h. Subsequently, 0.5 M NaCl (Sigma-Aldrich) was dissolved in the mixture, and the mixture was precipitated in a double volume of ethanol (Sigma-Aldrich). HAMA was then collected as white pellets after precipitation. The precipitate was washed with ethanol for 3 times before being dissolved in DI water and the solution was dialyzed against DI water for 5 d. The purified product was obtained by lyophilisation and stored at -20 °C until use.

2.1.1. DLP-based 3D printing system

The in-house DLP-based 3D printer consisted of a projector (ViewSonic PA503W), a custom-built ink vat, and a programmable, movable building platform [15, 51]. As shown in figure 1(a), the DMD chip (resolution: 1280×800 pixels) inside the projector projects printing patterns with visible light (25 mW cm⁻² of light intensity) onto the ink vat. The building platform allows us to obtain the 3D-printed construct via layer-by-layer photopolymerisation.

2.1.2. 3D printing methodology

Printing inks were prepared by mixing 40 vol.% poly(ethylene glycol)-di-acrylate (PEGDA, molecular weight (M_w) = 575 Da, Sigma-Aldrich), 15 wt.% GelMA, or 5 wt.% GelMA with 1.5 wt.% HAMA, 1 mM/10 mM tris(2,2-bipyridyl) dichlororuthenium (II) hexahydrate (Ru)/sodium persulfate (SPS)

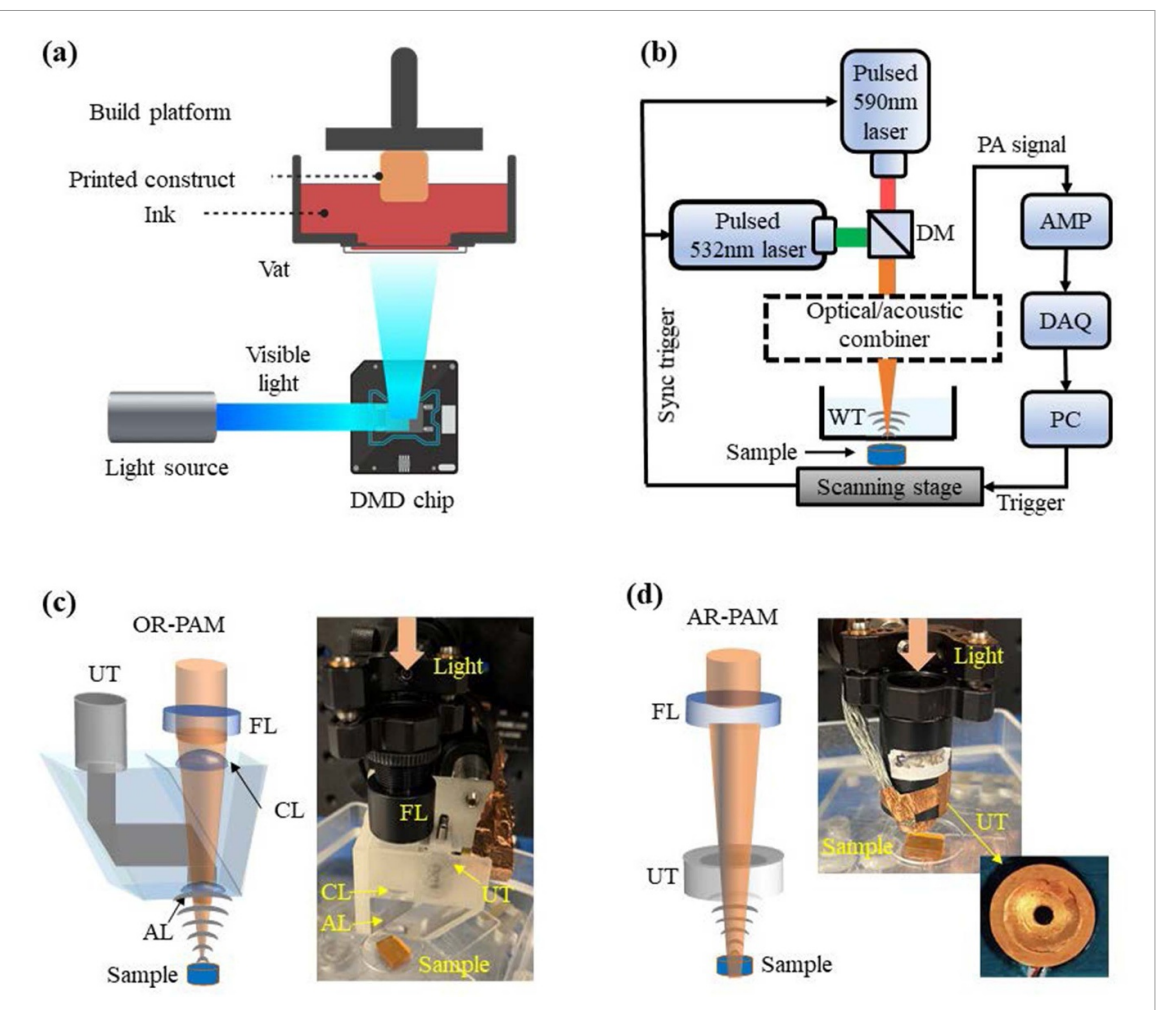


Figure 1. Principles of DLP-based 3D printing and PAM imaging. (a) Schematic of the DLP-based 3D-printing system. (b) Schematic of the PAM system with different optical-acoustic beam combining for OR-PAM or AR-PAM. AMP, amplifier; DAQ, data-acquisition; WT, water tank. (c) Schematic and photograph of optical-acoustic beam combiner for OR-PAM, with a silicone oil layer that transmits light and reflects sound. AL, acoustic lens; CL, correction lens; FL, focusing lens; UT, ultrasonic transducer. (d) Schematic and photograph of the optical-acoustic beam-combiner for AR-PAM, with a ring-shaped ultrasonic transducer.

(Advanced Biomatrix), and photoabsorber (Ponceau 4R, Sigma-Aldrich). Liquid inks were held in the vat with the Teflon AF 2400 film (50 μ m thickness, Random Technologies) at the bottom, which is hydrophobic and oxygen-permeable for decreasing material adhesion [52]. During printing, the build-platform was lowered to the first printing layer, and the ink was cured by a sequence of patterns at a speed of 10-70 μ m s⁻¹ and with a layer height of 200–350 μ m. Once the printing procedure was completed, the 3D constructs were carefully removed from the glass slide on the build-platform with a razor blade and washed with phosphate-buffered saline (PBS, Thermo Fisher). We used SolidWorks to design the printing models, sliced them with the opensource DLP slicer (https://formlabs.com/blog/opensource-dlp-slicer/, Formlabs), and finally loaded the sliced PNG images into our DLP-printing software.

2.1.3. PAM

In this study, we adapted our previously developed OR-PAM and AR-PAM systems, shown in figure 1(b).

In OR-PAM, the laser beam was tightly focused into a diffraction-limited spot, and the lateral resolution was primarily determined by the optical focal spot size [53]. OR-PAM has a limited penetration depth of \sim 1 mm with a lateral resolution of \sim 3.7 μ m, as shown in figure S1(a) (available online at stacks.iop.org/BF/14/025001/mmedia). Figure 1(c) is the schematic of the reflection-mode OR-PAM system. The excitation light was provided by a fiber laser (VPFL-G-20, Spectral Physics) at 532 nm and a dye laser (Credo, Sirah) at 590 nm. The laser beams were combined by a dichroic mirror (DMLP605, Thorlabs), focused by an objective lens, and delivered to the sample surface with a pulse energy of 800 nJ at 532 nm and 1.8 μ J at 590 nm. The resultant PA signals were then detected by an ultrasonic transducer with a central frequency of 30 MHz (V214-BB-RM, Olympus-NDT). Figure 1(d) is the schematic of the AR-PAM system, which can achieve a penetration depth beyond the ballistic regime. The light sources were the same as OR-PAM. The laser beams were weakly focused onto the sample surface with a pulse

energy of 1.7 μ J at 532 nm and 5.8 μ J at 590 nm. The resultant PA signals were then detected by a customized ring-shaped focused ultrasonic transducer with a central frequency of 20 MHz. The ring-shaped ultrasonic transducer has a central aperture to pass the excitation light. With acoustically defined lateral resolution, both ballistic and scattered photons that reach the target contribute to the final PA signals. The lateral resolution of the AR-PAM system is \sim 50 μ m, as shown in figure S1(b).

2.1.4. Blood clot preparation

Whole bovine blood was purchased from Lampire Biological Laboratories. 10 vol.% of 0.1 M CaCl₂ aqueous solution (Sigma-Aldrich) was added to the blood. The blood was mixed, drained into a centrifuge tube, and sealed for 20 min to induce clotting [54].

2.1.5. Blood-perfused microchannel with different oxygenation levels

The 3D-printed microchannel was sequentially perfused by blood with different oxygenation levels. The oxygenated whole bovine blood (7200 801, Lampire Biological Laboratories) was pumped with medical-grade nitrogen gas (NF200, Airgas) for 10 s, 1, 3 and 5 min, respectively, to achieve different oxygenation levels.

2.1.6. Measurement of absorption spectrum

The absorption spectrum of the photo-absorber (Ponceau 4R) was measured in the range of 380–740 nm using a microplate reader (SpectraMax M3, Molecular devices).

3. Results

3.1. Fabrication of vascular constructs using DLP-based 3D printing

Using the visible light-based DLP printer, 3D constructs were fabricated with the ink composed of 40 vol.% PEGDA ($M_w = 575 \text{ Da}$) and photoinitiator (1 mM/10 mM Ru/SPS), in the presence of photoabsorber (Ponceau 4R). Figure 2(a) illustrates the photo-polymerization process, in which the photons absorbed by the Ru/SPS promote their cleavage, resulting in the generation of free radicals. Ru/SPS, a visible-light photoinitiating system, has been used as an effective and biocompatible photoinitiator in numerous biomedical applications [55, 56]. The free radicals then react with the vinyl bonds in PEGDA to form the hydrogel. PEGDA is arguably the most commonly used synthetic material in DLP-based 3D printing, taking advantage of its good biocompatibility and proper mechanical properties that are needed for shape fidelity in 3D construction [12, 13, 57].

In DLP-based printing, except for the pixel size of the projector, the printing resolution also relies on the concentration of the photoabsorber, which limits the light penetration to achieve the desired printing layer thickness [13, 58]. In our printing platform, each pixel could be observed in the printed construct with the size of 60 μ m (figure S2). Additionally, we chose the red food coloring, Ponceau 4R, as the photoabsorber in our visible light-based system because of its high cytocompatibility and strong absorbance in the visible-light range (380–600 nm, figure 2(b)). The 2D vascular-like structures with 5–500 μ m-diameter branches were printed using inks containing 40 vol.% PEGDA ($M_w = 575 \text{ Da}$), 1 mM/10 mM Ru/SPS, and 0.0 wt.% to 2.0 wt.% Ponceau 4R. As shown in figures 2(c) and (d), in the absence of the photoabsorber, the branches smaller than 125 μ m could not be identified in the printed pattern, and the main vascular parts presented larger crosslinking areas likely because of the fast diffusion of the chemical species. After adding 1.0 wt.% or 1.5 wt.% photoabsorber into the ink, the printing fidelity was improved. Details of the branches could be observed in the construct printed with the ink containing 1.5 wt.% photoabsorber. However, some vascular branches disappeared when the photoabsorber was further increased to 2.0 wt.% due to insufficient crosslinking. Therefore, the inks with 1.0 wt.% and 1.5 wt.% Ponceau 4R were chosen to fabricate the 3D vascular constructs for subsequent PAM imaging and thrombosis studies.

We printed 3D vascular constructs (8, 6 and 4 mm in length, width, and height, respectively) with multivascular architectures with the total printing time of roughly 1 min each. After perfusing the microchannels with a water-soluble green dye (brilliant green, Sigma-Aldrich), the internal microchannels could be visualized from the photographs captured with a camera (figures 2(e) and S3). However, the water-soluble dye quickly diffused into the printed hydrogels, leading to the blurred edges of the microchannels observed in the images. To this end, we anticipated that the PAM systems could provide better imaging the 3D-printed constructs and detect the internal geometries.

3.2. OR-PAM imaging of the 3D-printed samples with the lower photoabsorber concentration

To obtain at high-resolution the structures of the 3Dprinted vascular constructs, we first applied OR-PAM to image the samples with 1.0 wt.% photo-absorber, which were relatively transparent and allowed the focused light penetrating deeper. Figure 3(a) shows the designs and photographs of three different printed structures that mimic various blood vessels, including the 'Y' structure, the 'single-loop' structure, and the 'double-loop' structure. Figure 3(b) shows the maximum amplitude projection (MAP) OR-PAM images of the three different patterns with the microchannels perfused by bovine whole blood, acquired at 532 nm. The microchannels inside the construct could be clearly imaged, shown in figure 3(c). The printed structures with the flat microchannels were clearly resolved. The depths of

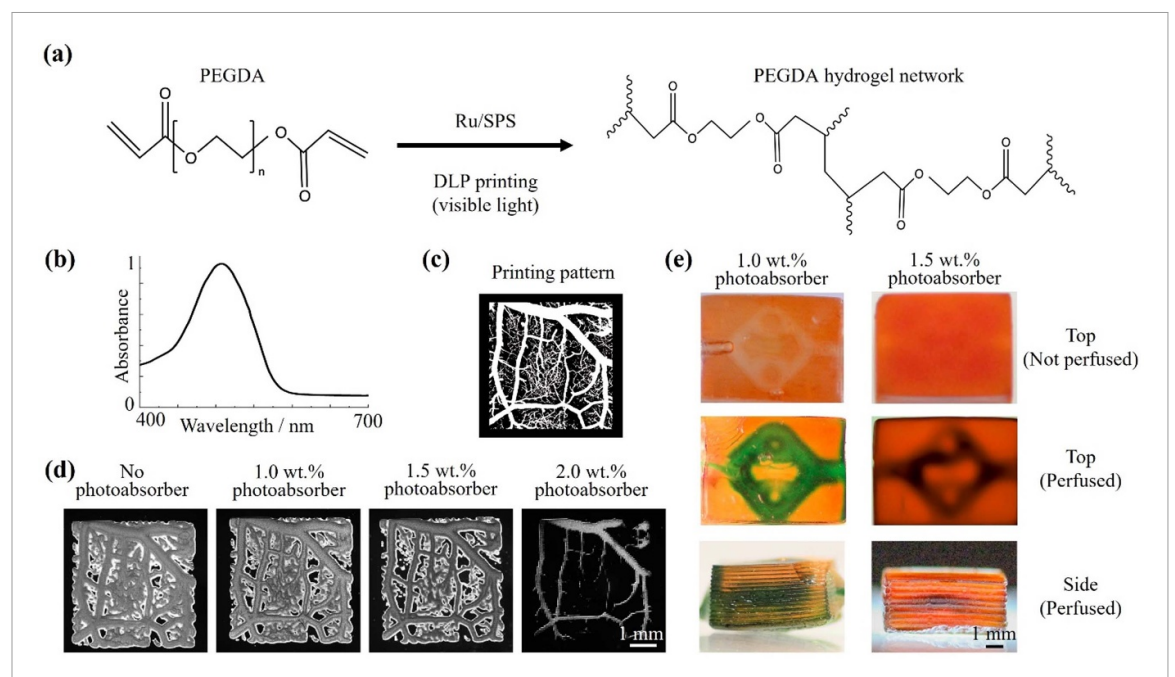


Figure 2. Fabrication of vascular constructs using DLP-based 3D printing. (a) The formation of PEGDA hydrogel through visible-light irradiation in the presence of Ru/SPS as photoinitiator. (b) The absorption spectrum of the photoabsorber (Ponceau 4R). (c) The designed digital printing pattern of a vascular network with branched structures. (d) Micrographs of printed 2D PEGDA samples containing different concentrations of photoabsorber. (e) Photographs of 3D constructs printed with 40 vol.% PEGDA ($M_w = 575 \, \text{Da}$), 1 mM/10 mM Ru/SPS, and 1.0 wt.% or 1.5 wt.% photoabsorber. The internal microchannels were perfused with a green dye to improve visibility.

the printed microchannels, which were 1.6 mm for the 'Y' structure, 1.3 mm for the 'single-loop' structure, and 1.7 mm for the 'double-loop' structure, respectively, could be accurately measured by the side-view MAP images. As shown in figure 3(d), the depth-coded images matched well with their corresponding side-view MAP images, which further demonstrated the 3D nature of these structures. As shown in the volumetric rendering videos S1–S3, OR-PAM was able to image not only the 3D-printed vascular microchannel perfused with blood, but also the printed hydrogel constructs due to the presence of the photo-absorber, which could be useful in evaluating the 3D-printing quality.

3.3. AR-PAM imaging of the 3D-printed samples with the higher photoabsorber concentration

Compared with 3D-printed samples containing the low-concentration photoabsorber (1.0 wt.%), the higher photo-absorber concentration (1.5 wt.%) could increase the sample's shape fidelity and is preferred for printing more sophisticated 3D structures. Two 3D-printed constructs both with 1.5 wt.% photo-absorber were initially fabricated for further PAM studies. As shown in figure 4(a), the samples printed with 1.5 wt.% photo-absorber were darker in color than those containing 1.0 wt.% photoabsorber (figure 3(a)), and were accordingly more difficult to identify their internal structures perfused by the blood. Because the higher photo-absorber concentration increases both the sample's absorption

and optical scattering, the samples could be effectively imaged by neither traditional optical microscopy, nor OR-PAM, as shown in figures 4(b) and S4(a). OR-PAM was not able to detect the sample's depth due to the low signal-to-noise ratio (SNR), as shown in figure S4(b).

To improve the penetration depth, we applied AR-PAM to image these samples printed with 1.5 wt.% photo-absorber, taking advantage of the deep penetration of the acoustic focusing. As expected, the samples with 1.5 wt.% photo-absorber could be clearly imaged by AR-PAM with blood perfusion, shown in figure 4(c). The internal microchannels were detected at various depths beyond 1 mm, shown in figure 4(d). The depth-coded images of the two constructs are shown in figure 4(e), demonstrating a 2.7 mm depth for the 'Y-shaped' structure and a 1.7 mm depth for the 'single-loop' structure. The volumetric renderings of the AR-PAM images are shown in videos S4 and S5.

Comparing the results obtained by OR-PAM and AR-PAM, we found that both the SNR and contrast of the AR-PAM images were substantially higher than those of the OR-PAM images. As shown in figure 4(f), the SNR of the AR-PAM image was 3.9 times higher than that of the OR-PAM image for the 'Y-shaped' structure and 3.8 times higher for the 'single-loop' structure. The contrast of the AR-PAM image was 12.8 times higher than that of the OR-PAM image for the 'Y-shaped' structure and 4.9 times higher for the 'single-loop' structure, as shown in figure 4(g). These

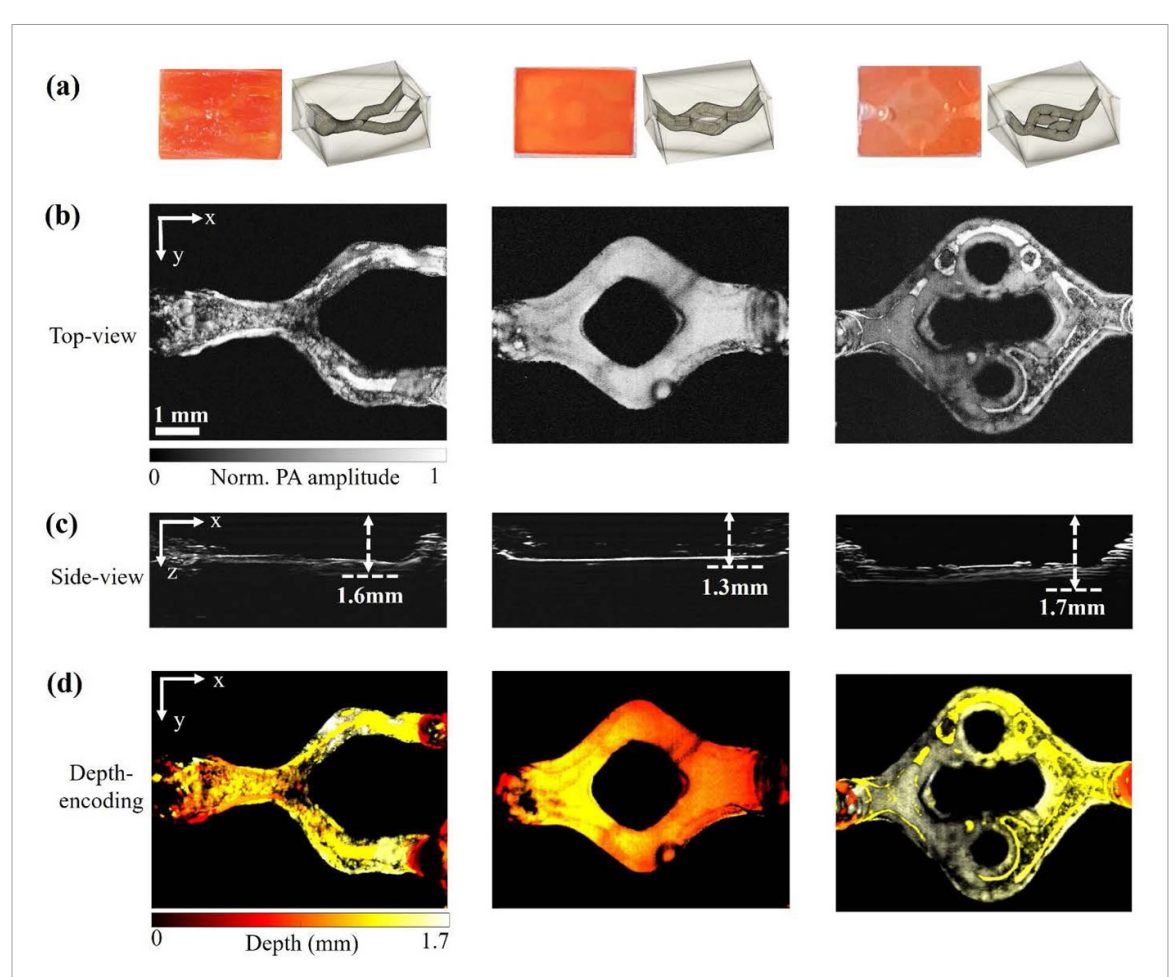


Figure 3. OR-PAM images of vascular constructs with 1.0 wt.% photoabsorber. (a) Photographs of three different types of printed 3D structures: Left: 'Y-shaped' structure; Middle: 'single-loop' structure; Right: 'double-loop' structure. (b) Corresponding top-view MAP images of the three constructs. (c) Corresponding side-view MAP images of the three constructs. (d) Corresponding depth-coded images of the three constructs.

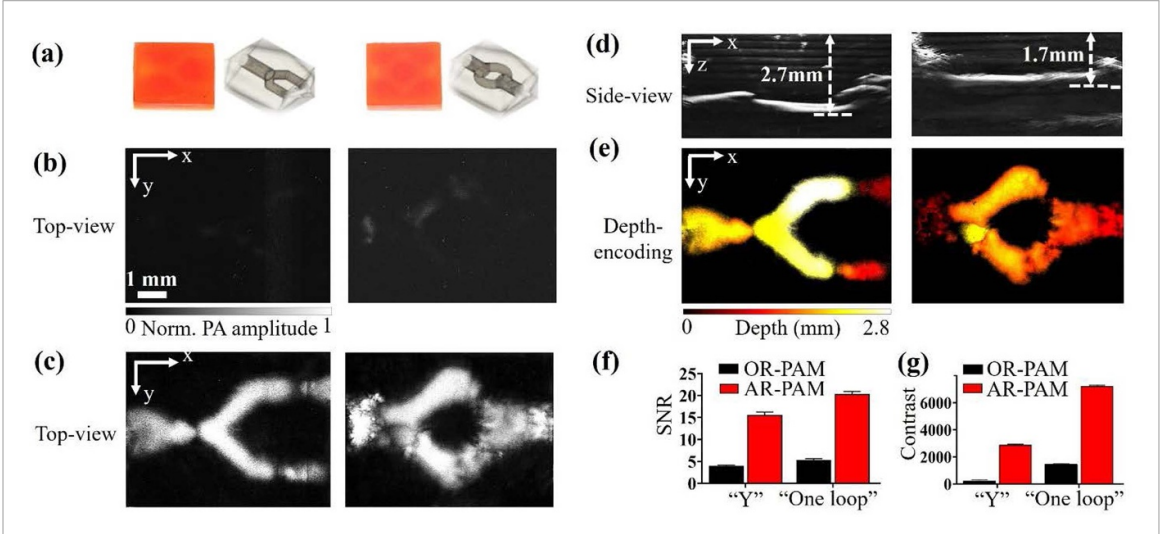


Figure 4. AR-PAM images of vascular constructs printed with 1.5 wt.% photoabsorber. (a) Photographs of two printed structures: Left, 'Y-shaped' structure; Right, 'single-loop' structure. (b) Corresponding top-view MAP images of the two structures acquired by OR-PAM. (c) Corresponding top-view MAP images of the two structures acquired by AR-PAM. (d) Corresponding side-view MAP images acquired by AR-PAM. (e) Corresponding depth-coded images acquired by AR-PAM. (f) Comparisons of SNRs and (g) contrasts of the structures imaged by OR-PAM and AR-PAM.

results demonstrated that AR-PAM performed better than OR-PAM in imaging the 3D-printed samples containing higher photo-absorber concentrations.

We further demonstrated the applicability of our PAM systems for imaging 3D objects printed with additional biomaterials. GelMA has been widely

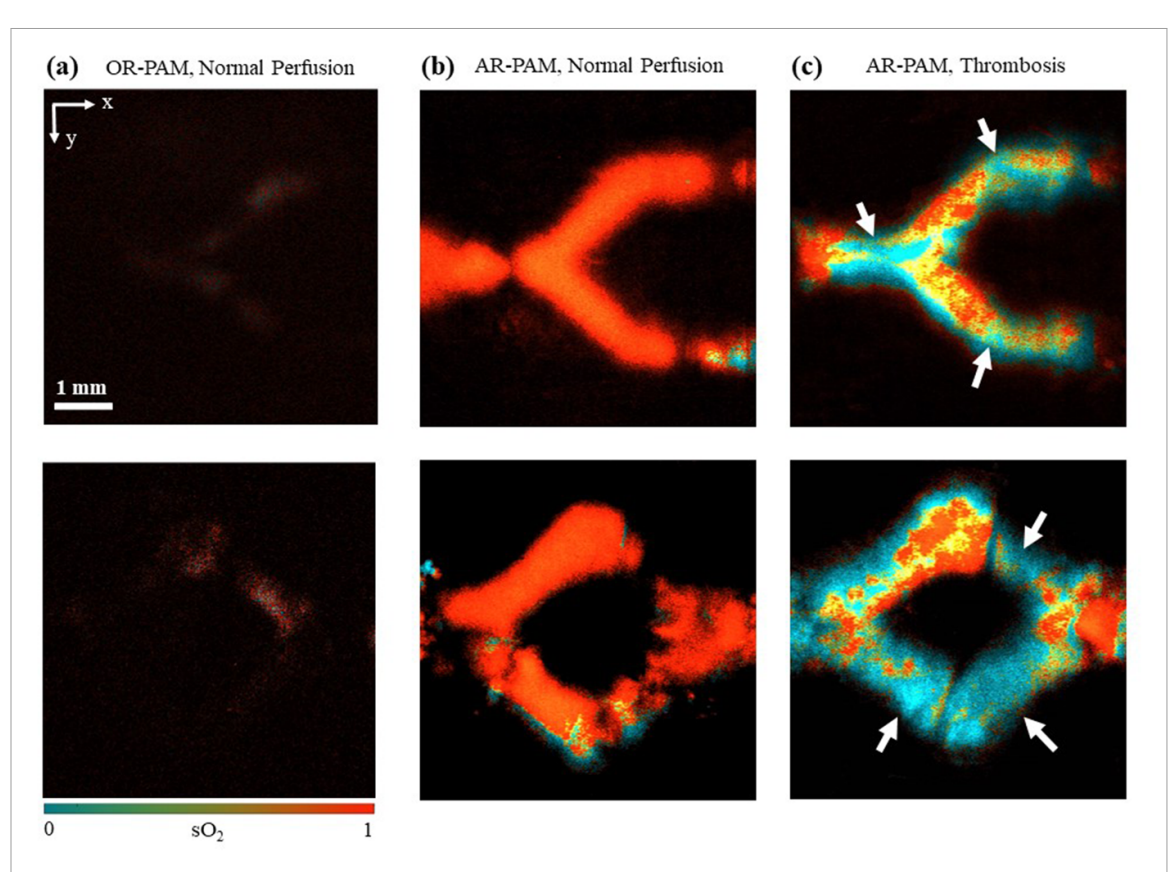


Figure 5. Comparison of the sO₂ images obtained by OR-PAM and AR-PAM on two 3D-printed structures. Top row, 'Y-shaped' structure; Bottom row, 'single-loop' structure. (a) OR-PAM sO₂ images of samples perfused with oxygenated blood. (b) AR-PAM sO₂ images of the samples perfused with oxygenated blood. (c) AR-PAM sO₂ images of the samples filled with closts. The arrows point to some representative thrombi.

applied for light-assisted bioprinting due to the abundant intrinsic bioactive moieties for cell adhesion [59]. We prepared the ink consisted of 15 wt.% GelMA, 1 mM/10 mM Ru/SPS, and 1.5 wt.% photoabsorber, and printed 3D structures at the speed of $20~\mu m \, s^{-1}$. We also formulated the mixture of GelMA and HAMA as another ink. As shown in figure S6, the 'single-loop' microchannel structures printed using GelMA and GelMA/HAMA-based inks were also successfully imaged by AR-PAM, with comparable qualities of the constructs printed with PEGDA.

3.4. Functional imaging of the 3D-printed thrombosis models

Blood oxygenation is an important indicator of tissue hypoxia and can be used for characterizing the thrombi that typically feature low oxygenation [60, 61]. The oxygen saturation of hemoglobin (sO₂) can be computed by using multi-wavelength measurement [62]. In this work, we used two wavelengths at 532 and 590 nm for sO₂ measurement on 3D-printed vascular constructs with 1.5 wt.% photoabsorber. Indeed, we demonstrated that AR-PAM was capable of measuring the sO₂ change in a printed vascular sample sequentially perfused with blood at different oxygenation levels ranging from 0.93–0.55, as shown in figure S5. Of note, figure 5(a) shows the sO₂

images of the 'Y-shaped' and 'single-loop' constructs filled with oxygenated bovine whole blood, acquired by OR-PAM. Again, it was challenging for OR-PAM to provide accurate sO₂ measurement if possible at all, due to the limited penetration depth. By contrast, the sO₂ images acquired by AR-PAM clearly showed the uniformly high oxygenation level of the internal microchannels, as shown in figure 5(b).

To demonstrate the functional imaging capability of AR-PAM on thrombosis models, we perfused the 3D-printed vascular constructs and induced in situ blood clotting within the microchannels and quantified the sO2 in the microchannels. As shown in figure 5(c), the thrombi had a much lower oxygenation level compared with the normal blood, which is consistent with the previously published results [63, 64]. The arrows pointed out in figure 5(c) are some representative thrombus locations. During the blood clot formation, the oxygen content inside the clot is reduced due to the lack of effective oxygen exchange with the surrounding medium [14, 41, 63], which was efficiently reproduced in our 3D-printed vascular models. From figure 5(c), we could also observe that a thrombus could form in both the relatively flat microchannels and the sloped inlet/outlet, demonstrating the accurate 3D localization provided by AR-PAM.

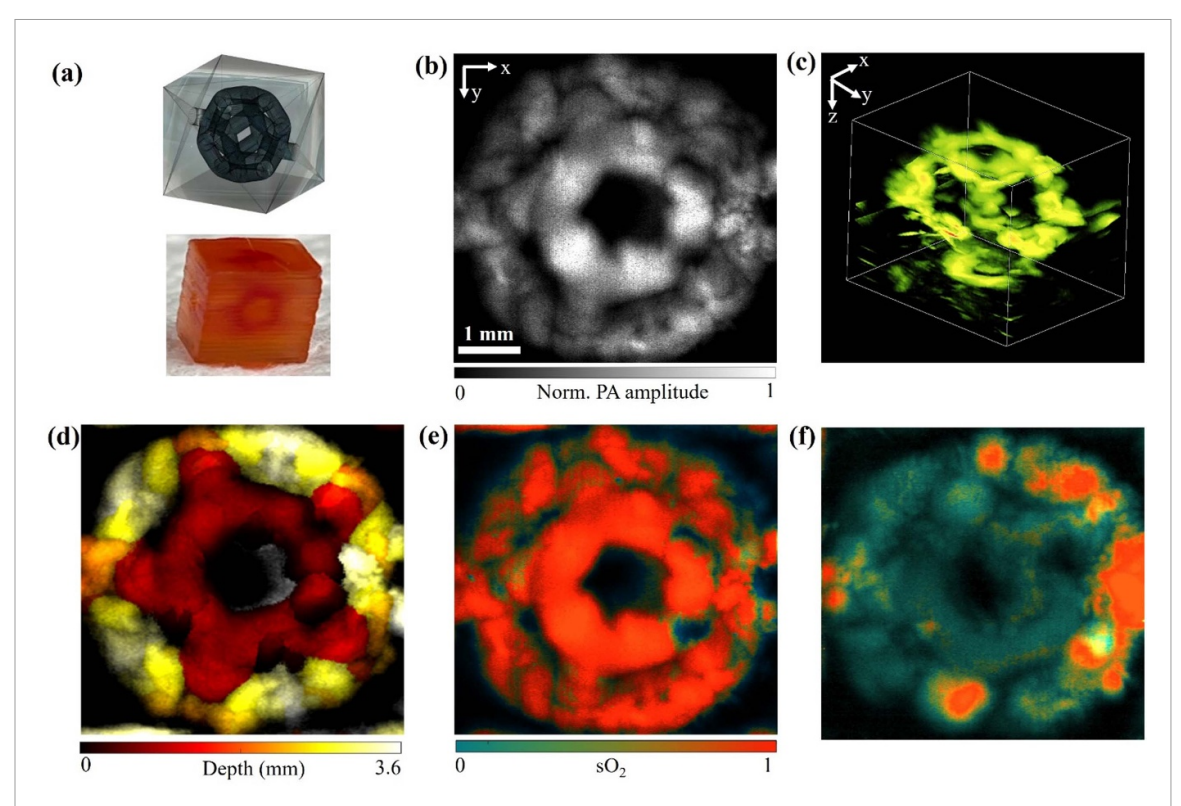


Figure 6. AR-PAM of a 3D-printed geometrically complex dodecahedron-patterned microchannel structure. (a) Design and photograph of the geometrically complex dodecahedron-patterned microchannel structure. (b) Top-view and (c) 3D-view AR-PAM MAP images of the structure perfused with bovine whole blood. (d) Depth-coded image. (e), (f) sO_2 images of the structure (e) perfused with oxygenated blood and (f) filled with thrombus.

3.5. AR-PAM image of geometrically complex microchannel structures

As discussed above, the 3D constructs printed with 1.5 wt.% photo-absorber exhibit better shape fidelity that can support the production of more complex microchannel structures than those containing lower photo-absorber concentrations. Therefore, we printed a geometrically complex 3D structure featuring embedded dodecahedron-patterned microchannels with the dodecahedron diameter of 3.6 mm, as shown in figure 6(a). The dodecahedron-patterned microchannels could not be imaged by traditional optical microscopy, but AR-PAM was able to access the entire volume, as shown in video S6. Figures 6(b) and (c) show the top-view and 3D-view MAP AR-PAM images, respectively, of the dodecahedronpatterned microchannels, demonstrating the deep penetration of 3.6 mm. The sophisticated volumetric structure of the dodecahedron-patterned microchannels was clearly depicted by the depth-coded image, as shown in figure 6(d). A thrombosis study was also performed on these constructs. As shown in figures 5(e) and (f), AR-PAM was able to quantity the sO2 levels over the entire dodecahedronpatterned microchannel configuration, showing that the thrombi formed in the sample had a much lower oxygenation level than the normal blood. These results have strongly suggested that AR-PAM is capable of imaging complex 3D-printed structures otherwise

not possible with most conventional imaging tools at sufficient resolution and sensitivity.

4. Discussions and conclusion

Many cardiovascular diseases, such as myocardial infarction and ischemic stroke, are caused by thrombosis [5]. 3D-printed vascular constructs containing complex microchannel geometries can provide a powerful platform for in vitro thrombosis studies [54, 65]. However, it is difficult for traditional optical imaging to observe the internal structures within bulky hydrogels, mainly because of three reasons: (1) the photo-absorber (or other components) used in 3D printing, in particular DLP printing, is typically non-fluorescent and thus cannot be detected by fluorescence imaging; (2) the 3D-printed sample are usually thick, especially when printing more complex structures. The traditional optical imaging cannot image the thick samples because of the limit of the penetration depth even if there exist intrinsic fluorescence contrasts; and (3) more sophisticated structures can be printed by DLP printing with the addition of more photo-absorber, but the photo-absorber will further bring in stronger optical absorption that limit the penetration of ballistic photons. Combining rich optical contrast and deep acoustic penetration, PAM is a highly promising solution.

To the best of our knowledge, this study has demonstrated the first application of PAM in imaging 3D-printed vascular structures. PAM, especially AR-PAM, can overcome the penetration limit of traditional optical microscopy and image the complex 3D-printed vessel models. Our experimental results have shown that OR-PAM could clearly image the 3D-printed constructs with 1.0 wt.% photo-absorber but not those with 1.5 wt.% photo-absorber, suggesting its limited penetration depth when the absorption of the samples is increased. AR-PAM could image samples with 1.5 wt.% photo-absorber, benefiting from its large penetration depth. Complex structures such as the geometrically complex dodecahedronpatterned microchannels could be imaged by AR-PAM with a penetration depth of at least 3.6 mm. Furthermore, AR-PAM was able to quantify the sO_2 levels of deep structures, which is useful for identifying the hypoxic thrombi from the surrounding blood.

There are two major technical limitations in this study. The first limitation is that the imaging speeds of both OR-PAM and AR-PAM systems currently used are relatively slow due to the point-by-point raster scanning performed with the motorizes scanning stages. The typical scanning speed was 5 mm s⁻¹ and it usually took more than 15 min to image one sample in this study. It is not fast enough to monitor the hemodynamics or the formation of the thrombosis in real time. Nevertheless, the imaging speed can be readily improved by developing high-speed PAM systems using faster scanning mechanisms such as the polygon scanner [66] or the micro-electromechanical system (MEMS) scanner [67, 68]. Another limitation is that the lateral resolution of PAM decreases with the penetration depth. For OR-PAM, the lateral resolution is determined by the size of the optical focus, which enlarges due to the light scattering at larger depths. For AR-PAM, the lateral resolution is determined by the size of the acoustic focus, which is inversely proportional to the central frequency of the PA signal. Due to the frequency-dependent acoustic attenuation in samples, the high-frequency signals are attenuated more than the low frequency signals. Therefore, the signals from the deeper regions have lower frequencies, leading to reduced resolutions.

It needs to be further noted that the minimal blood vessel resolution we may achieve in this study was mainly determined by the resolution of the 3D printing method, since the imaging resolutions (3.8 μ m for OR-PAM and 28 μ m for AR-PAM) were finer than the printer resolution. The resolutions of DLP-based 3D printing are different in the x-y plane and along the z dimension. In the x-y plane, the resolution primarily depends on the pixel size of the DMD projecting the light patterns and the accessary projecting optics. The DMD chip (1280 \times 800 pixels) inside our DLP printer projects patterns at a 38 μ m resolution onto the ink vat after

the magnification by the optical system. Additionally, the stepper motor's step size (5 μ m in our printing system) and the light penetration depth are the key factors that determine the z resolution. In this study, we chose Ponceau 4R as the photo-absorber due to its strong absorption within the visible-light spectrum and the negligible toxicity. We previously observed reduced curing size and crosslinking thickness in inks with higher concentrations of the photoabsorber (Ponceau 4R), which suggests that increasing the concentration of Ponceau 4R can reduce the optical penetration depth and thus achieve better structural precision and higher circularity of the printed channel [7, 12, 24]. The photo-absorber (Ponceau 4R) concentration applied in our 3D printing was 1.5 wt.% in most cases, resulting in the minimum diameter of 0.5 mm for the printed microchannels. The light penetration depth and channel diameter can be decreased by adding more photo-absorber, but the absorption by the photo-absorber may decrease the imaging depth of PAM.

In summary, we have demonstrated that PAM may provide a practically useful platform for imaging 3D-printed vascular structures. These vessel models allow us to develop a variety of disease models beyond thrombosis. The functional measurements by PAM in deep and complex structures present a unique opportunity for understanding disease development and even treatment efficacies. Future work includes longitudinal monitoring of the thrombosis-formation in the microchannels over time, and multi-spectral analysis of the clot composition (e.g. lipid, fibrin, hemoglobin). We expect that the integration of PAM with 3D printing/bioprinting will likely enable numerous applications in tissue engineering and tissue model engineering, and can be readily expanded to other tissue types.

Data availability statement

All data that support the findings of this study are included within the article (and any supplementary files).

Acknowledgments

We thank Dr. Caroline Connor for editing the manuscript. This work was sponsored by American Heart Association Collaborative Sciences Award (18CSA34080277); Duke Institute of Brain Science Incubator Award; the United States National Institutes of Health (NIH) Grant Nos. R21EB027981, R21EB027304, R21EB026175, R21EB030257, RF1NS115581 (BRAIN Initiative), R00CA201603, R01NS111039, R01EB028143, UG3TR003274; the United States National Science Foundation (NSF) CBET-EBMS-1936105; Chan Zuckerberg Initiative Grant (2020-226178); Brigham Research Institute.

ORCID iDs

Chenshuo Ma https://orcid.org/0000-0001-9701-2566

Luis Santiago Mille https://orcid.org/0000-0001-7072-1522

Yu Shrike Zhang https://orcid.org/0000-0002-0045-0808

Junjie Yao 6 https://orcid.org/0000-0002-2381-706X

References

- DeCherney A and Berkowitz G 1982 Thrombosis and acute coronary-artery lesions in sudden cardiac ischemic death New Engl. J. Med. 310 1137–40
- [2] Mai C and Hunt D 2011 Upper-extremity deep venous thrombosis: a review *Am. J. Med.* 124 402–7
- [3] Bick R L 2003 Cancer-associated thrombosis New Engl. J. Med. 349 109–11
- [4] Lloyd-Jones D et al 2010 Heart disease and stroke statistics—2010 update: a report from the American heart association Circulation 121 948–54
- [5] Engelter S T, Fluri F, Buitrago–Téllez C, Marsch S, Steck A J, Rüegg S and Lyrer P A 2005 Life-threatening orolingual angioedema during thrombolysis in acute ischemic stroke J. Neurol. 252 1167–70
- [6] Mackman N 2008 Triggers, targets and treatments for thrombosis *Nature* 451 914–8
- [7] Wang M et al 2021 Digital light processing based bioprinting with composable gradients Adv. Mater. 34 2107038
- [8] Murphy S V, De Coppi P and Atala A 2020 Opportunities and challenges of translational 3D bioprinting *Nat. Biomed.* Eng. 4 370–80
- [9] Heinrich M A *et al* 2019 3D bioprinting: from benches to translational applications *Small* 15 1–47
- [10] Sasmal P, Datta P, Wu Y and Ozbolat I T 2018 3D bioprinting for modelling vasculature *Microphysiol. Syst.* 1 1
- [11] Zhang Y S *et al* 2017 3D bioprinting for tissue and organ fabrication *Ann. Biomed. Eng.* **45** 148–63
- [12] Li W et al 2021 A smartphone-enabled portable digital light processing 3D printer Adv. Mater. 33 1–10
- [13] Grigoryan B et al 2019 Multivascular networks and functional intravascular topologies within biocompatible hydrogels Science 364 458–64
- [14] Das D and Pramanik M 2019 Combined ultrasound and photoacoustic imaging of blood clot during microbubble-assisted sonothrombolysis J. Biomed. Opt. 24 1
- [15] Garciamendez-Mijares C E, Agrawal P, García Martínez G, Cervantes Juarez E and Zhang Y S 2021 State-of-art affordable bioprinters: a guide for the DiY community Appl. Phys. Rev. 8 031312
- [16] Wang M, Li W, Tang G, Garciamendez-Mijares C E and Zhang Y S 2021 Engineering (Bio)materials through shrinkage and expansion Adv. Healthcare Mater. 10 2100380
- [17] Hwang H H, Zhu W, Victorine G, Lawrence N and Chen S 2018 3D-printing of functional biomedical microdevices via light- and extrusion-based approaches Small Methods 2 1–18
- [18] Shumer D E and N. J. N. N. P. S 2017 Recent advances in formulating and processing biomaterial inks for vat polymerization-based 3D printing *Physiol. Behav.* 176 139–48
- [19] Nagla D M 2016 Aqueous two-phase emulsion bioink-enabled 3D bioprinting of porous hydrogels *Physiol. Rehaw* 176 100-6
- [20] Melchels F P W, Feijen J and Grijpma D W 2010 A review on stereolithography and its applications in biomedical engineering *Biomaterials* 31 6121–30
- [21] Kinstlinger I S and Miller J S 2016 3D-printed fluidic networks as vasculature for engineered tissue *Lab Chip* 16 2025–43

- [22] Goyanes A, Det-Amornrat U, Wang J, Basit A W and Gaisford S 2016 3D scanning and 3D printing as innovative technologies for fabricating personalized topical drug delivery systems J. Control. Release 234 41–48
- [23] Ye W et al 2020 3D printing of gelatin methacrylate-based nerve guidance conduits with multiple channels Mater. Des. 192 108757
- [24] Levato R et al 2021 High-resolution lithographic biofabrication of hydrogels with complex microchannels from low-temperature-soluble gelatin bioresins Mater. Today Bio 12 100162
- [25] Zhang Y S, Wang L V and Xia Y 2016 Seeing through the surface: non-invasive characterization of biomaterial–tissue interactions using photoacoustic microscopy Ann. Biomed. Eng. 44 649–66
- [26] Zhang Y S and Yao J 2018 Imaging biomaterial—tissue interactions *Trends Biotechnol.* **36** 403–14
- [27] Wang L V and Yao J 2016 A practical guide to photoacoustic tomography in the life sciences Nat. Methods 13 627–38
- [28] Yao J and Wang L V 2013 Photoacoustic microscopy Laser Photon. Rev. 7 758–78
- [29] Cox B, Laufer J G, Arridge S R and Beard P C 2012 Quantitative spectroscopic photoacoustic imaging: a review J. Biomed. Opt. 17 061202
- [30] Zhang Y et al 2011 Noninvasive photoacoustic microscopy of living cells in two and three dimensions through enhancement by a metabolite dye Angew. Chem. 123 7497–501
- [31] Zhang Y S, Yao J, Zhang C, Li L, Wang L V and Xia Y 2014 Optical-resolution photoacoustic microscopy for volumetric and spectral analysis of histological and immunochemical samples Angew. Chem. 126 8237–41
- [32] Strohm E M, Moore M J and Kolios M C 2016 Single cell photoacoustic microscopy: a review *IEEE J. Sel. Top.* Quantum Electron. 22 137–51
- [33] Zhang H F, Maslov K and Wang L V 2007 In vivo imaging of subcutaneous structures using functional photoacoustic microscopy Nat. Protocols 2 797–804
- [34] Jeon S, Song H B, Kim J, Lee B J, Managuli R, Kim J H, Kim J H and Kim C 2017 *In vivo* photoacoustic imaging of anterior ocular vasculature: a random sample consensus approach *Sci. Rep.* 7 1–9
- [35] Wong T T W et al 2017 Label-free automated three-dimensional imaging of whole organs by microtomy-assisted photoacoustic microscopy Nat. Commun. 8 1386
- [36] De Liao L et al 2010 Imaging brain hemodynamic changes during rat forepaw electrical stimulation using functional photoacoustic microscopy Neuroimage 52 562–570
- [37] Stein E W, Maslov K and Wang L V 2009 Noninvasive, in vivo imaging of blood-oxygenation dynamics within the mouse brain using photoacoustic microscopy J. Biomed. Opt. 14 020502
- [38] Chen S-L, Xie Z, Carson P L, Wang X and Guo L J 2011 In vivo flow speed measurement of capillaries by photoacoustic correlation spectroscopy Opt. Lett. 36 4017
- [39] Sheinfeld A and Eyal A 2012 Photoacoustic thermal diffusion flowmetry Biomed. Opt. Express 3 800
- [40] Brunker J and Beard P 2016 Velocity measurements in whole blood using acoustic resolution photoacoustic Doppler Biomed. Opt. Express 7 2789
- [41] Das D, Sivasubramanian K, Rajendran P and Pramanik M 2020 Label-free high frame rate imaging of circulating blood clots using a dual modal ultrasound and photoacoustic system J. Biophoton. 14 1–10
- [42] Weber J, Beard P C and Bohndiek S E 2016 Contrast agents for molecular photoacoustic imaging *Nat. Methods* 13 639–50
- [43] Nie L, Chen M, Sun X, Rong P, Zheng N and Chen X 2014 Palladium nanosheets as highly stable and effective contrast agents for *in vivo* photoacoustic molecular imaging *Nanoscale* 6 1271–6

- [44] Pu K, Shuhendler A J, Jokerst J V, Mei J, Gambhir S S, Bao Z and Rao J 2014 Semiconducting polymer nanoparticles as photoacoustic molecular imaging probes in living mice Nat. Nanotechnol. 9 233–9
- [45] Homan K A, Souza M, Truby R, Luke G P, Green C, Vreeland E and Emelianov S 2012 Silver nanoplate contrast agents for *in vivo* molecular photoacoustic imaging ACS Nano 6 641–50
- [46] Cai X et al 2012 Multi-scale molecular photoacoustic tomography of gene expression PLoS One 7 e43999
- [47] Jeon M, Kim J and Kim C 2016 Multiplane spectroscopic whole-body photoacoustic imaging of small animals in vivo Med. Biol. Eng. Comput. 54 283–94
- [48] Maharjan S et al 2021 Symbiotic photosynthetic oxygenation within 3D-bioprinted vascularized tissues Matter 4 217–40
- [49] Sharifi F et al 2020 A hepatocellular carcinoma—bone metastasis-on-a-chip model for studying thymoquinone-loaded anticancer nanoparticles Bio-Des. Manuf. 3 189–202
- [50] Gong J et al 2020 Complexation-induced resolution enhancement of 3D-printed hydrogel constructs Nat. Commun. 11 1–14
- [51] Miri A K et al 2018 Microfluidics-enabled multimaterial maskless stereolithographic bioprinting Adv. Mater. 30 1–9
- [52] Tumbleston J R et al 2015 Continuous liquid interface production of 3D objects Science 347 1349–52
- [53] Maslov K, Zhang H F, Hu S and Wang L V 2008 Optical-resolution photoacoustic microscopy for in vivo imaging of single capillaries Opt. Lett. 33 929
- [54] Zhang Y S et al 2016 Bioprinted thrombosis-on-a-chip Lab Chip 16 4097–105
- [55] Bertlein S et al 2017 Thiol—ene clickable gelatin: a platform bioink for multiple 3D biofabrication technologies Adv. Mater. 29 1703404
- [56] Lim K S et al 2019 Visible light cross-linking of gelatin hydrogels offers an enhanced cell microenvironment with improved light penetration depth *Macromol. Biosci.* 19 1900098
- [57] Mau R, Nazir J, John S and Seitz H 2019 Preliminary study on 3D printing of PEGDA hydrogels for frontal sinus

- implants using digital light processing (DLP) *Curr. Dir. Biomed. Eng.* 5 249–52
- [58] Ge L, Dong L, Wang D, Ge Q and Gu G 2018 A digital light processing 3D printer for fast and high-precision fabrication of soft pneumatic actuators Sens. Actuators A 273 285–92
- [59] Ying G, Jiang N, Yu C and Zhang Y S 2018 Three-dimensional bioprinting of gelatin methacryloyl (GelMA) Bio-Des. Manuf. 1 215–24
- [60] Hennen S N et al 2015 Photoacoustic tomography imaging and estimation of oxygen saturation of hemoglobin in ocular tissue of rabbits Exp. Eye Res. 138 153–8
- [61] Leach R M and Treacher D F 1998 Oxygen transport—2. Tissue hypoxia Clin. Rev. 317 1370–3
- [62] Yao J, Wang L, Yang J-M, Maslov K I, Wong T T W, Li L, Huang C-H, Zou J and Wang L V 2015 High-speed label-free functional photoacoustic microscopy of mouse brain in action *Nat. Methods* 12 407–10
- [63] Karpiouk A B, Aglyamov S R, Mallidi S, Shah J, Scott W G, Rubin J M and Emelianov S Y 2008 Combined ultrasound and photoacoustic imaging to detect and stage deep vein thrombosis: phantom and ex vivo studies J. Biomed. Opt. 13 054061
- [64] Nakase H, Heimann A and Kempski O 1996 Alterations of regional cerebral blood flow and oxygen saturation in a rat sinus-vein thrombosis model Stroke 27 720–8
- [65] Costa P F et al 2017 Mimicking arterial thrombosis in a 3D-printed microfluidic: in vitro vascular model based on computed tomography angiography data Lab Chip 17 2785–92
- [66] Lan B et al 2018 High-speed widefield photoacoustic microscopy of small-animal hemodynamics Biomed. Opt. Express 9 4689
- [67] Chen M, Duan X, Lan B, Vu T, Zhu X, Rong Q, Yang W, Hoffmann U, Zou J and Yao J 2021 High-speed functional photoacoustic microscopy using a water-immersible two-axis torsion-bending scanner *Photoacoustics* 24 100309
- [68] Yao J, Wang L, Yang J-M, Gao L S, Maslov K I, Wang L V, Huang C-H and Zou J 2012 Wide-field fast-scanning photoacoustic microscopy based on a water-immersible MEMS scanning mirror J. Biomed. Opt. 17 1